C. R. Physique 17 (2016) 1027–1037

Contents lists available at ScienceDirect

Comptes Rendus Physique

www.sciencedirect.com

Probing matter with electromagnetic waves / Sonder la matière par les ondes électromagnétiques

Superposition of fiber Bragg and LPG gratings for embedded strain measurement

Réseau de Bragg et réseau longue période superposés pour la mesure de déformation au cœur des matériaux

Romain Guyard, Dominique Leduc *, Yann Lecieux, Cyril Lupi

Institut de génie civil et de mécanique (GeM), l'UNAM Université, Université de Nantes, UMR CNRS 6183, 2, rue de la Houssinière, 44322 Nantes, France

ARTICLE INFO

Article history:
Available online 11 August 2016

Keywords:
Strain
Embedded sensors
Optical fiber gratings

Mots-clés :
Déformation
Capteurs enfouis
Réseaux fibrés

ABSTRACT

When a fiber Bragg grating strain sensor is embedded inside a structure, the interaction of the sensor with the host material can lead to spurious results if the radial strain is neglected. In this article, we use numerical simulations to show that the axial and radial strains can be simultaneously measured with a single fiber in which a Bragg grating and a long-period grating are superimposed. Moreover, we present an optimal architecture of the sensor.

RÉSUMÉ

Une nouvelle architecture de capteur de déformations à fibre optique basée sur la superposition d'un réseau de Bragg et d'un réseau longue période est proposée afin de mesurer, à partir de deux signaux linéairement indépendants, les déformations transverse et longitudinale dans un milieu hôte. Un dimensionnement du capteur est réalisé par résolution numérique des conditions de résonance des réseaux ; il est démontré la possibilité d'évaluer simultanément ces déformations sans altération de la précision des mesures par rapport aux capteurs de déformation à fibre optique classiques.

1. Introduction

Fiber Bragg gratings (FBG) are made of periodic modulations of the refractive index of the core of an optical fiber. As a consequence, they behave as bandpass filters and reflect a very narrow spectral band of the incoming light, centered on the

* Corresponding author.
E-mail address: dominique.leduc@univ-nantes.fr (D. Leduc).

http://dx.doi.org/10.1016/j.crhy.2016.07.014

Bragg wavelength: $\lambda_B = 2n_{eff}\Lambda_0$, where n_{eff} is the effective index of the light propagating inside the core and Λ_0 the period of the grating. Any change in the period of the grating or in the effective index induces a shift in the Bragg wavelength.

FBGs are often used as strain sensors (see, for example, [1–5]). Indeed, when the fiber is strained, the period of the grating is modified. Moreover, due to the photo-elastic effect, the effective index also varies:

$$\frac{\Delta\lambda_B}{\lambda_B} = \frac{\Delta n_{eff}(\bar{\bar{\varepsilon}})}{n_{eff}} + \frac{\Delta\Lambda}{\Lambda} \tag{1}$$

What should be underlined is that the variation of the effective index depends on the strains in all directions:

$$\Delta\left(\frac{1}{n_{ij}^2}\right) = p_{ijkl}\varepsilon_{kl} \qquad (i,j,k,l = 1,2,3) \tag{2}$$

where p_{ijkl} are the components of the photo-elastic tensor and ε_{kl} the components of the strain tensor $\bar{\bar{\varepsilon}}$. For a classic optical fiber, when the strain is isotropic in the cross section of the sensor, and under the approximation that the effective index change is the same as the change in the index of the bulk material:

$$\frac{\Delta n_{eff}}{n_{eff}} = -\frac{n_{eff}^2}{2}\left[(p_{11}+p_{12})\varepsilon_r + p_{12}\varepsilon_z\right] \tag{3}$$

where $\varepsilon_r = \varepsilon_{11} = \varepsilon_{22}$ is the radial strain and $\varepsilon_z = \varepsilon_{33}$ the axial strain [6,7].

When the fiber is glued at two points on the surface of the monitored structure, its *axial* strain, ϵ_z, is exactly the same as the strain of the structure. Moreover, as the fiber is free to deform in the transverse plane, its *radial* strain ϵ_r is driven by the axial strain: $\epsilon_r = -\nu\epsilon_z$, where ν is the Poisson's ratio of the fiber. In this case, the axial strain is the only unknown and the measurement of a single Bragg wavelength shift is then sufficient:

$$\frac{\Delta\lambda_B}{\lambda_B} = \frac{\Delta n_{eff}}{n_{eff}} + \varepsilon_z = \left\{1 - \frac{n_{eff}^2}{2}\left[p_{12} - \nu(p_{11}+p_{12})\right]\right\}\varepsilon_z \tag{4}$$

This is why FBG strain sensors are usually mounted at the surface of the structure. Equation (4) is the classical relation between Bragg wavelength shift and strain.

When the fiber is embedded, it is not free anymore to deform in the transverse plane. Its radial strain then depends in a non-trivial manner on the interaction between the fiber and the host material. It can not be deduced simply from the axial strain. Then the axial and the radial strains must be simultaneously determined. This implies that two linearly independent measurements have to be performed at the same point, which in turn requires specific sensors. In order to measure these two unknown strains, several architectures are possible. Among them, the most encouraging ones are based on: the superposition of two FBG of different periods [8], the use of a Bragg grating written in a birefringent optical fiber [9,10], and the superposition of a FBG and a LPG [11–13]. Nevertheless, the sensor made up of superimposed long-period and short-period Bragg gratings appears to be the only one to have a resolution on the axial strain measurement similar to the resolution of FBG strain gage [14].

The first section is devoted to the study of the limits of the classical relation (4) between the Bragg wavelength shift and strain. This study underlines the need for a new architecture of embedded sensors. So, in the second section, we study numerically the efficiency of an architecture made of the superposition of a long- and of a short-period grating [14]. Then we look for configurations that can fulfill the following requirements:

- the sensor has to measure simultaneously the radial and axial strains with the same precision on the axial strain as the FBGs mounted on surface, i.e. 1 $\mu\epsilon$;
- the transmission spectrum of the sensor has to exhibit only two peaks in the range [1400 nm; 1600 nm], one associated with the FBG and one to the Long-Period Grating (LPG) in order to avoid any ambiguity in the order of the mode of the LPG;
- the response of the sensor must be linear in the range $\varepsilon_{r,z} \in [-5000\ \mu\epsilon; +5000\ \mu\epsilon]$.

2. The need for a simultaneous measurement of axial and radial strains

2.1. Single fiber in uniaxial tension

When the fiber submitted to a uniaxial tension is free to become deformed in the transverse plane, the radial and axial strains are linked by the Poisson ratio. However, even in this case, equation (3) is an approximation. It is right for the refractive index of the core n_1 and the refractive index of the cladding n_2, but not for n_{eff}, since n_{eff} is not the index of a bulk material, but an effective index. Indeed, the light inside an optical fiber propagates in the core and also in the cladding. Then, it experiences a refractive index, which is neither the index of the core nor the index of the cladding, but somewhere in between.

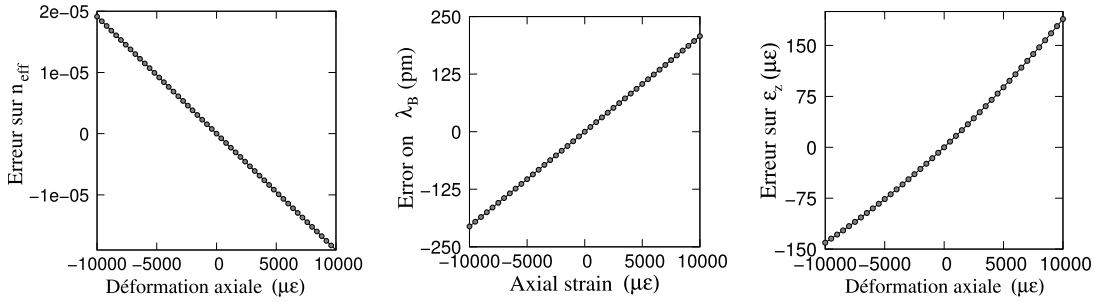

(a) Error on the effective index. (b) Error on the Bragg wavelength. (c) Error on the axial strain.

Fig. 1. Fiber in uniaxial tension.

By solving the Maxwell equations in the fiber with appropriate boundary conditions, one shows that n_{eff} is the solution to:

$$F_c(a_1, n_1, n_2, \lambda) = qK_0(q)J_1(h) - hJ_0(h)K_1(q) = 0 \text{ with } h = u_1\sqrt{n_1^2 - n_{\text{eff}}^2} \text{ and } q = u_1\sqrt{n_{\text{eff}}^2 - n_2^2} \tag{5}$$

where J and K are Bessel functions, a_1 is the core radius, and $u_1 = 2\pi a_1/\lambda$. As we can see, n_{eff} depends on both the material characteristics and the geometry of the fiber.

When the fiber is strained, the refractive indices of the core and the cladding vary according to equation (3) and the change in the core radius is $\Delta a_1/a_1 = -\nu\varepsilon_z$. The exact associated variation of n_{eff} must be calculated thanks to equation (5) using the modified indices and radius. Fig. 1a shows the difference between the exact effective index and the approximation given by equation (3) for a SMF28 fiber ($n_1 = 1.4496$; $n_2 = 1.4444$; $a_1 = 4.2$ µm) at 1550 nm. The maximum is approximately $2{\cdot}10^{-5}$ for a 10000-µϵ axial strain.

For FBG, an error of 10^{-5} on the effective index induces an error of ten picometers on the Bragg wavelength. This corresponds to about ten µϵ according to equation (4). But, as a matter of fact, there is another source of inaccuracy in this equation. Indeed, in the resonance equation of Bragg wavelength, n_{eff} depends on the Bragg wavelength itself via the dispersion equation (5). In order to retrieve the right Bragg wavelength, one has to take into account the variations of the characteristics of the fiber with the wavelength. In the transparency regions, the variations of n_2 are well described by a Sellmeier law:

$$n_2^2(\lambda) = 1 + \sum_{j=1}^{N} A_j \left(1 - \lambda_j^2/\lambda^2\right)^{-1} \tag{6}$$

where A_j and λ_j are material parameters. We will subsequently use the coefficients of quenched SiO_2 [15]. The index of the core is given and $n_1 = 1.0036n_2$.

In order to determine λ_{B0}, that is the Bragg wavelength of the grating at rest, the resonance condition is used to substitute n_{eff0}, the effective index at rest by its expression as a function of λ_{B0}: $n_{\text{eff0}} = \lambda_{B0}/(2\Lambda_0$ in the parameters h and q of equation (5), which is solved in λ_{B0} by using a bisection method.

The same procedure is used when the grating is strained, with the following parameters: $\Lambda = \Lambda_0(1 + \varepsilon_z)$, $a_1 = a_{10}(1 - \nu\varepsilon_z)$ and $n_i(\lambda) = n_{i0}(\lambda) - n_{i0}^3(\lambda)\,[p_{12} - \nu(p_{11} + p_{12})]\,\varepsilon_z/2$ where $i = \{1, 2\}$.

Fig. 1b shows the difference between the Bragg wavelength computed thanks to expressions (4) and (3) and the real one calculated with the previous method. The error can reach several hundred picometers, because the variations of n_1 and n_2, and consequently of n_{eff}, are of the order of 10^{-4} when the wavelength changes by few nanometers. This leads to a significant error on the strain: as shown by Fig. 1c, it is close to 200 µϵ for an axial strain of 10000 µϵ.

As a conclusion, the relations (4) and (3) are approximated, even for the bare fiber submitted to uniaxial tension. Their relative accuracy is of the order of 2%. If one wants to eliminate this source of uncertainty without being obliged to determine the intrinsic characteristics of the fiber, one has to calibrate the response of the fiber as a function of the strain.

2.2. Fiber embedded in transversally isotropic composite materials in uniaxial tension

Once the fiber is embedded in a part, there is a mechanical coupling between the sensor and the studied material. In order to understand how the fiber becomes deformed, we study the problem of two concentric cylinders in uniaxial tension (see Fig. 2). The central cylinder of radius R_i corresponds to the sensor while the hollow cylinder of external radius R_e corresponds to the host material. The fiber is uncoated; consequently the material chosen to model the fiber is a homogeneous and isotropic cylinder of silica. The host material is a transversally isotropic composite material oriented in the same direction as the reinforcement fibers (as shown in Fig. 2). Then, in the rest of this paper, the quantities superscripted f stand for the FBG, while those superscripted h stand for the host material.

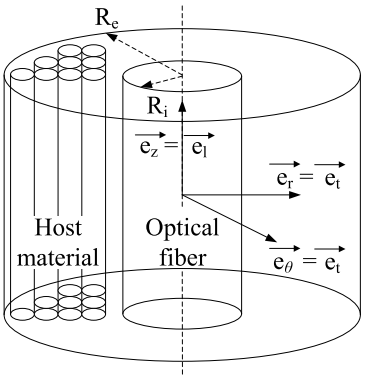

(a) Specimen instrumented with an optical fiber sensor: geometry.

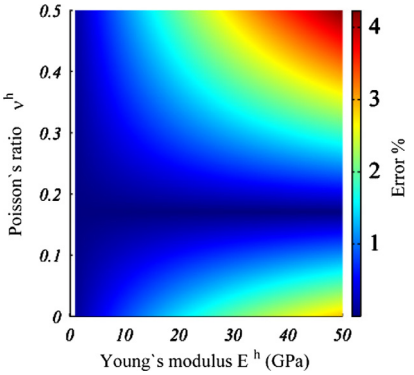

(b) Difference between the classical model and the model taking into account the mechanical coupling between the host material and the optical fiber sensor.

Fig. 2. Analysis of FBG axial strain taking into account the effect of the mechanical coupling due to the strain of host material exerted on the fiber in the radial direction.

The displacement field $\vec{u}$ in the fiber and in the external cylinder is written as (see [16]:

$$\vec{u}^{\mathrm{f,h}} = \begin{cases} u_r^{\mathrm{f,h}}\,\vec{e_r} \\ u_z^{\mathrm{f,h}}\,\vec{e_z} \end{cases} = \begin{cases} C^{\mathrm{f,h}} r + \frac{D^{\mathrm{f,h}}}{r}\,\vec{e_r} \\ K^{\mathrm{f,h}} z\,\vec{e_z} \end{cases} \tag{7}$$

where r is the radial cylindrical coordinate, while $C^{\mathrm{f,h}}$, $D^{\mathrm{f,h}}$ and $K^{\mathrm{f,h}}$ are constants given by the boundary conditions of the problem. With the displacement field, we obtain the strain tensor such as: $\bar{\bar{\varepsilon}} = \frac{1}{2}(\nabla\vec{u} + \nabla\vec{u}^{\mathrm{T}})$ and then the stress tensor with: $\bar{\varepsilon} = \bar{\bar{D}}\ \bar{\sigma}$ with $\bar{\varepsilon} = \langle \varepsilon_{zz}, \varepsilon_{rr}, \varepsilon_{\theta\theta}, \sqrt{2}\varepsilon_{r\theta}, \sqrt{2}\varepsilon_{z\theta}, \sqrt{2}\varepsilon_{zr}\rangle^{\mathrm{T}}$, $\bar{\sigma} = \langle \sigma_{zz}, \sigma_{rr}, \sigma_{\theta\theta}, \sqrt{2}\sigma_{r\theta}, \sqrt{2}\sigma_{z\theta}, \sqrt{2}\sigma_{zr}\rangle^{\mathrm{T}}$ and $D_{ij} = 0$ except $D_{11} = 1/E_{\mathrm{l}} = D_{22} = D_{33} = 1/E_{\mathrm{t}}$, $D_{12} = D_{13} = D_{21} = D_{31} = -\nu_{\mathrm{lt}}/E_{\mathrm{l}}$, $D_{23} = D_{32} = -\nu_{\mathrm{tt}}/E_{\mathrm{t}}$, $D_{44} = (1 + \nu_{\mathrm{tt}}/E_{\mathrm{t}}$ and $D_{55} = D_{66} = 1/(2G)$, where the subscript l stands for the longitudinal direction $\vec{e_z}$ while t stands for the transverse directions (which are in the plane of the fiber cross section).

A uniform tensile strain is imposed on the specimen $\varepsilon_z \approx \sigma_z^{\mathrm{h}}/E_{\mathrm{l}}^{\mathrm{h}}$, but it remains free to move in the radial direction. The boundary conditions allowing us to calculate the six unknown constants are the following:

(i) no radial displacement at $r = 0$ $u_r^{\mathrm{f}}(0) = 0 \Rightarrow D^{\mathrm{f}} = 0$;
(ii) equality of the axial displacement $u_z^{\mathrm{f}} = u_z^{\mathrm{h}} \Rightarrow K^{\mathrm{f}} = K^{\mathrm{h}} = \varepsilon_z$; we assume a perfect bonding between the optical fiber and the host material. This assumption was verified experimentally before [17];
(iii) continuity of the radial displacement at the interface between the FBG and the specimen $u_r^{\mathrm{h}}(R_{\mathrm{i}}) = u_r^{\mathrm{f}}(R_{\mathrm{i}}) \Rightarrow C^{\mathrm{h}} R_{\mathrm{i}} + \frac{D^{\mathrm{h}}}{R_{\mathrm{i}}} = C^{\mathrm{f}} R_{\mathrm{i}}$;
(iv) continuity of the radial stress at the interface $\sigma_{rr}^{\mathrm{f}}(R_{\mathrm{i}}) = \sigma_{rr}^{\mathrm{h}}(R_{\mathrm{i}})$
(v) no radial stress on the specimen external surface $\sigma_{rr}^{\mathrm{h}}(R_{\mathrm{e}}) = 0$.

The radial strain of the optical fiber thus computed is a function of R_{e} and R_{i}, the external and internal radii of the instrumented specimen. In order to generalize this result to any geometry of the host structure, the following hypothesis is made: $R_{\mathrm{i}}^2/R_{\mathrm{e}}^2 \simeq 0$. This implies that: $\varepsilon_r^{\mathrm{f}} = C^{\mathrm{f}} \approx -\kappa\varepsilon_z$ where:

$$\kappa = \frac{-\nu^{\mathrm{f}}E^{\mathrm{f}} - \nu^{\mathrm{f}}E^{\mathrm{f}}\nu_{\mathrm{tt}} - \nu_{\mathrm{tl}}E_{\mathrm{l}} + \nu_{\mathrm{tl}}E_{\mathrm{l}}\nu^{\mathrm{f}} + 2\nu_{\mathrm{tl}}E_{\mathrm{l}}(\nu^{\mathrm{f}})^2}{-E^{\mathrm{f}} - E^{\mathrm{f}}\nu_{\mathrm{tt}} - E_{\mathrm{t}} + E_{\mathrm{t}}\nu^{\mathrm{f}} + 2E_{\mathrm{t}}(\nu^{\mathrm{f}})^2} \tag{8}$$

For isotropic materials, $\nu_{\mathrm{tt}} = \nu_{\mathrm{tl}} = \nu^{\mathrm{h}}$ and $E_{\mathrm{l}} = E_{\mathrm{t}} = E^{\mathrm{h}}$, where ν^{h} is the Poisson ratio of the host material and E^{h} its Young modulus. One can notice that in this case, if $\nu^{\mathrm{f}} = \nu^{\mathrm{h}}$ then $\kappa = \nu^{\mathrm{f}}$ as expected.

Equation (8) shows that the radial strain $\varepsilon_r^{\mathrm{f}} = C^{\mathrm{f}} \approx -\kappa\varepsilon_z$ is really constant in the sensor, but that it is not equal to $-\nu^{\mathrm{f}}\varepsilon_z$. There is a mechanical coupling between the strain in the specimen and that in the fiber. Consequently, the strain in the fiber depends on the material properties in which it is embedded. Thus, using equation (3) and considering $\varepsilon_r^{\mathrm{f}} = -\nu\varepsilon_z$ fails to estimate ε_z. The error done depends on the properties of the couple of materials used for the specimen and the optical fiber. Fig. 2 allows us to estimate it when the host material is homogeneous. It shows the relative difference between ε_z, calculated with the approximated relation: $\varepsilon_r^{\mathrm{f}} = -\nu^{\mathrm{f}}\varepsilon_z$ and ε_z calculated with the correct relation: $\varepsilon_r^{\mathrm{f}} = -\kappa\varepsilon_z$ for a given value of $\frac{\Delta\lambda}{\lambda}$ (calculated with $p_{11} = 0.113$, $p_{12} = 0.252$, $n_{\mathrm{eff}} = 1.447467$ [18]). In order to draw this figure, we have settled the following material properties for the optical fiber: $\nu^{\mathrm{f}} = 0.17$ and $E^{\mathrm{f}} = 70000$ MPa. For a fixed Poisson

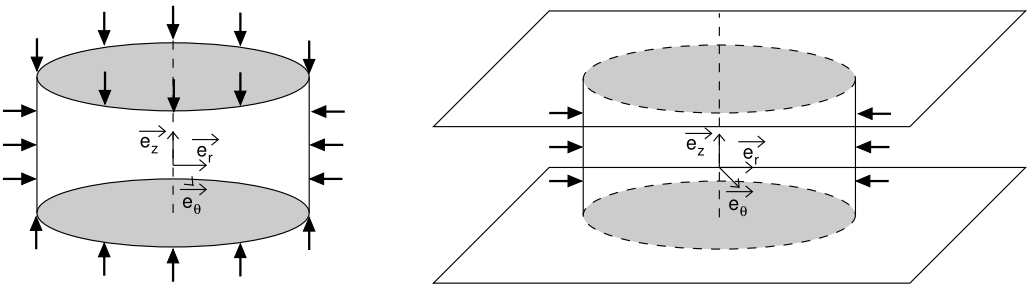

(a) free cylinder (b) fixed sections

Fig. 3. The two different boundary conditions for the cylinder in thermal load analysis.

Table 1
Difference between the real strains and the strains measured by a single FBG.

	Free cylinder		Fixed sections	
	Axial strain	Radial strain	Axial strain	Radial strain
Calcul	-11400 μϵ	1562 μϵ	0 μϵ	-438 μϵ
FBG	-11200 μϵ	X	209 μϵ	X

ratio, the higher the Young's modulus of the host material is, the more important it is to consider the effect of the radial strain exerted on the sensor. Thus, the effect of the radial strain on the measurement of an FBG axial strain will be nearly negligible if it is embedded in a pure polyester resin. Conversely, this phenomenon could lead to substantial errors in the interpretation of the FBG axial strain in materials such as fiber-charged resins or in transversally isotropic composites. More than 1% of error is done using ν_f instead of κ in equation (1) in the case of an epoxy ($E = 3.1$ GPa, $\nu = 0.4$) carbon fiber transversally isotropic composite ($E = 130$ GPa, $\nu = 0.4$ [19]) containing 75 percent fiber by volume.

Different ways of performing an accurate measurement with an embedded FBG are available, taking into account the effect of the radial strain on the shift of Bragg wavelength:

- to perform an experimental calibration of the sensor [20], which implies to use exactly the same materials as in the final environment;
- to use the previous analytical model, which implies having a thorough knowledge of E^h and ν^h;
- to know ε_r and use the relations (3) and (1).

The last method requires a sensor capable of measuring simultaneously the radial and the axial strains, as described in section 2.

2.3. Thermal loads

We will now consider a fiber embedded in a heat-hardening resin as used in the composite material. We suppose that a FBG has been set up in the mold before resin injection. The initially liquid resin is heated and becomes solid. During cooling, it imposes a mechanical stress on the fiber axially as well as radially. This case should happen in production process monitoring. The following study focuses only on the post-cure process. At this stage, the resin is in a solid state, but it keeps on cooling down. In spite of the temperature change, the stiffness and the strength of the resin do not evolve anymore. Consequently, its Poisson's coefficient and its Young's modulus may be assumed unchanging.

We assume that the FBG is embedded in a 20-mm-diameter epoxy resin cylinder whose Young modulus is 3100 MPa, Poisson ratio is 0.4, and thermal expansion coefficient is $114{\cdot}10^{-6}$ K^{-1}. A drop of 100 K in temperature is imposed on the structure. As in the previous problem, the displacement and strain field are given by relation (7). Nevertheless, the Hooke's law includes here an additional term relative to the thermal change, i.e.

$$\bar{\bar{\sigma}} = \lambda tr(\bar{\bar{\varepsilon}})\bar{\bar{I}} + 2\mu\bar{\bar{\varepsilon}} - (3\lambda + 2\mu)\alpha\Delta T\bar{\bar{I}} \tag{9}$$

where α is the thermal expansion coefficient, $\mu = \frac{E}{2(1+\nu)}$ and $\lambda = \frac{\nu E}{(1-2\nu)(1+\nu)}$ are the Lamé coefficients.

Two different boundary conditions are considered here (cf. Fig. 3). Firstly, the cylinder is free to undergo axial and radial deformations. In the second case, the radial surface is free, while the upper and lower sections are fixed. Table 1 shows the values of the axial strain obtained if the Bragg wavelength shift is analyzed with equation (4) expanded with a term related to the thermal change. For the cylinder free to undergo axial and radial deformations, the analysis of the wavelength shift according to equation (4) and the additional term $a\Delta T$ provide an axial strain ε_z of -11234 μϵ, which gives a relative error of 1.45% with the real strain of -11400 μϵ. For the cylinder with fixed upper and lower sections, the drop of 100 K in

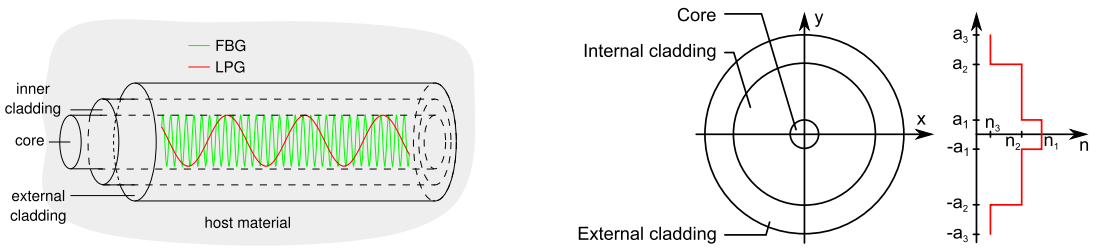

Fig. 4. Geometry of sensor. The red and green lines represent the variation of the refractive index of the core corresponding to the LPG and the FBG.

temperature causes a radial strain $\varepsilon_r^{\mathrm{h}} = -15960\ \mu\epsilon$ in the resin and $\varepsilon_r^{\mathrm{f}} = -438\ \mu\epsilon$ in the FBG, and therefore a shift in the Bragg wavelength of -0.974 nm. The analysis of this data using relation (4) leads us to conclude that the FBG undergoes an axial extension of 209 $\mu\epsilon$, while it actually undergoes a purely radial strain.

Of course, the two previous case studies are purely academic. The real difficulty in the analysis of optical signals for applications in production process monitoring is that the boundary conditions are very seldom well known. So the real boundary conditions would not probably be the same as in any of the two cases studied here, which shows the necessity to measure both the axial and radial strains.

3. The dual grating sensor

3.1. Architecture of the sensor

The sensor is made of the juxtaposition of two gratings of same length inside the core of a fiber, surrounded by two concentric claddings (see Fig. 4). Both gratings can be written using UV light with the same phase mask technique. The best is to write first the Bragg grating with one mask and then the long-period grating with another mask [21]. This procedure enables us to superimpose these two gratings without degrading their spectral response [13].

We call a_1 the radius of the core and n_1 its refractive index, a_2 the radius of the inner cladding and n_2 its index, and a_3 the radius of the external cladding and n_3 its index. So that only one mode propagates in the core of the fiber, the coefficients a_1, n_1 and n_2 are fixed at the same values as those of a classical SMF28 fiber, as in section 2.

The first grating is a classical fiber Bragg grating. It reflects a narrow bandwidth of the incoming light centered on the Bragg wavelength λ_{B}. As a consequence, its transmission spectrum exhibits a hole around λ_{B}. The value of λ_{B} is given by the condition of resonance:

$$\lambda_{\mathrm{B}} = 2n_{\mathrm{eff}}^{\mathrm{core}}\left(a_1,\ n_1,\ n_2, \lambda_{\mathrm{B}}\right)\Lambda_{\mathrm{B}} \tag{10}$$

where Λ_{B} is the period of the grating and $n_{\mathrm{eff}}^{\mathrm{core}}$ the effective index of the mode that propagates inside the core. It is given by the dispersion equation [22]:

$$F_c\left(a_1, n_1, n_2, n_{\mathrm{eff}}^{\mathrm{core}}, \lambda\right) = 0 \tag{11}$$

The second grating is a long-period grating that couples the mode inside the core to resonant inner cladding modes. The wavelengths of resonant cladding modes are given by:

$$\lambda_{\mathrm{LPG}} = \left[n_{\mathrm{eff}}^{\mathrm{core}}\left(a_i,\ n_i, \lambda_{\mathrm{LPG}}^m\right) - n_{\mathrm{eff,m}}^{\mathrm{clad}}\left(a_i,\ n_i, \lambda_{\mathrm{LPG}}^m\right)\right]\Lambda_{\mathrm{LPG}} \tag{12}$$

where Λ_{LPG} is the period of the grating and $n_{\mathrm{eff,m}}^{\mathrm{clad}}$ the effective index of the mth cladding mode. It is given by the dispersion equation of the cladding modes [22]:

$$F_g\left(a_1, a_2, n_1, n_2, n_3, n_{\mathrm{eff}}^{\mathrm{core}}, n_{\mathrm{eff}}^{\mathrm{clad}}, \lambda\right) = 0 \tag{13}$$

The light propagating inside the cladding gradually vanishes because of inhomogeneities and micro-bending. The transmission spectrum of the LPG exhibits then holes around each λ_{LPG}.

The coupling coefficient κ^m between a cladding mode m and the core mode [23]:

$$\kappa^m = \frac{\omega\epsilon_0 n_1^2}{2}\int_0^{2\pi} \mathrm{d}\theta \int_0^{a_1} r\mathrm{d}r\ E_{\mathrm{t}}^m \cdot E_{0t}^* \tag{14}$$

gives the strength of the coupling and then the depth of the hole in the spectrum.

3.2. Principle of the measurement

When the fiber is strained, the period of the gratings, the radii and the indices of the three layers change. The variation of the period of each grating depends on the axial strain: $\Lambda = (1+\epsilon_z)\,\Lambda_0$, where Λ_0 is the period of the grating at rest, while the changes of the radii depend on the radial strain: $a_i = (1+\epsilon_r)\,a_{0i}$ for $i = \{1,2,3\}$, where a_{0i} is the radius at rest of the layer i. The variation of the refractive indices depends on both strains, due to the photo-elastic effect: $n_i = n_{i0} - n_{i0}^3\,[(p_{11}+p_{12})\,\epsilon_r + p_{12}\epsilon_z]/2$ for $i = \{1,2,3\}$, where $p_{11} = 0.113$, $p_{12} = 0.252$ are the components of the photo-elastic tensor of silica [18]. According to equations (11) and (13), the variations of the radii and of the refractive indices induce a variation of the effective indices of the core mode and of the cladding modes. All these changes cause a shift in λ_B and λ_{LPG}, which can be expressed in the linear regime as the first system given by equation (15), where α_{1r} and α_{1z} are respectively the sensitivity of the FBG to the radial and axial strain, and α_{2r} and α_{2z} are respectively the sensitivity of the LPG to the radial and axial strains. In a real experiment, one would measure these two shifts in wavelength and deduce the strains by inverting this system:

$$\begin{cases} \Delta\lambda_B &= \alpha_{1r}\epsilon_r + \alpha_{1z}\epsilon_z \\ \Delta\lambda_{LPG} &= \alpha_{2r}\epsilon_r + \alpha_{2z}\epsilon_z \end{cases} \Rightarrow \begin{cases} \epsilon_z &= \dfrac{\alpha_{1r}\Delta\lambda_{LPG} - \alpha_{2r}\Delta\lambda_B}{D} \\ \epsilon_r &= \dfrac{\alpha_{2z}\Delta\lambda_B - \alpha_{1z}\Delta\lambda_{LPG}}{D} \end{cases} \tag{15}$$

where $D = \alpha_{1r}\alpha_{2z} - \alpha_{2r}\alpha_{1z}$.

The smallest measurable axial $\Delta\epsilon_z$ and radial $\Delta\epsilon_r$ strains can be derived from (15) using an uncertainty calculation:

$$\begin{cases} \Delta\epsilon_z &= \dfrac{|\alpha_{1r}| + |\alpha_{2r}|}{|D|}\delta\lambda_{min} \\ \Delta\epsilon_r &= \dfrac{|\alpha_{1z}| + |\alpha_{2z}|}{|D|}\delta\lambda_{min} \end{cases} \tag{16}$$

where $\delta\lambda_{min}$ is the smallest measurable wavelength shift. It is usually of the order of 1 pm. Equation (16) shows that the largest D is, the better the resolution is.

3.3. Method to determine optimal architecture

The aim of the study is to find an architecture that meets the specifications described in the Introduction. The parameters are a_1, a_2, a_3, n_1, n_2, n_3, λ_B, and λ_{LPG}. The number of parameters can be reduced with the help of physical considerations. As stated above, the characteristics of the core and the refractive index of the inner cladding are chosen to be the same as those of a single-mode SMF28 fiber. The outer cladding serves to isolate the modes of the inner cladding from the environment of the fiber. Its radius must be sufficiently large so that the cladding modes amplitudes fall to zero well before the interface between the outer cladding and the external medium. In practice, $a_3 = a_2 + 15$ µm is enough. In contrast, the refractive index of the outer cladding n_3 influences very little the properties of the grating. It can be arbitrarily chosen in the range $[1.; n_2[$. We use the value $n_3 = 0.95\,n_2$, which is compatible with silica. The period of the Bragg grating is fixed at 501 nm in order to obtain a Bragg wavelength of 1.45 µm. Finally, the only free parameters are a_2 and Λ_{LPG}.

In order to determine the best couples of parameters $\{a_2, \Lambda_{LPG}\}$, we proceeded to a systematic exploration of the parameters' space, with Λ_{LPG} varying from 100 µm to 500 µm by steps of 5 µm, and a_2 varying from 15 µm to 70 µm by steps of 0.5 µm. Values of a_2 smaller than 15 µm were not considered because in this case the inner cladding is not large enough to isolate the core mode from the outer cladding.

For each couple $\{a_2, \Lambda_{LPG}\}$, we first determined the wavelength of the resonant cladding modes of the unstrained sensor using (11), (12), and (13). We only kept the couples for which only one mode was present in the range [1400 nm, 1600 nm]. Then we applied a radial strain comprised in the range $[-5000\ \mu\epsilon; +5000\ \mu\epsilon]$, the axial strain remaining null. For each strain, the new radii and indices were calculated with the help of (11) and (13). This led to the new values of λ_B and λ_{LPG}, from which were deduced the shifts $\Delta\lambda_B$ and $\Delta\lambda_{LPG}$. Then a linear regression gave the sensitivity α_{1r} of the Bragg wavelength and α_{2r} of the long-period grating to the radial strain. The same procedure was used to calculate the sensitivity of the FBG and of the LPG to the axial strain.

4. Results

Fig. 5 shows a cartography of the coupling coefficient κ and of the parameter D for the first five odd cladding modes, as a function of a_2 and Λ_{LPG}. Even modes are not considered since their coupling coefficient is almost zero.

The white areas in each graph correspond to configurations where λ_{LPG} is outside the range [1400 nm; 1600 nm]. For each mode and for both D and κ, the shape of the colored area looks like a comma, which tip is close to the lowest Λ_{LPG} and the lowest a_2. Above mode 5, the tip is split into two parts, with a dead zone where no mode falls in the desired range. The sign of D changes through the critical zone and the coupling coefficient abruptly falls to zero. This corresponds to a change in the modal properties of the cladding.

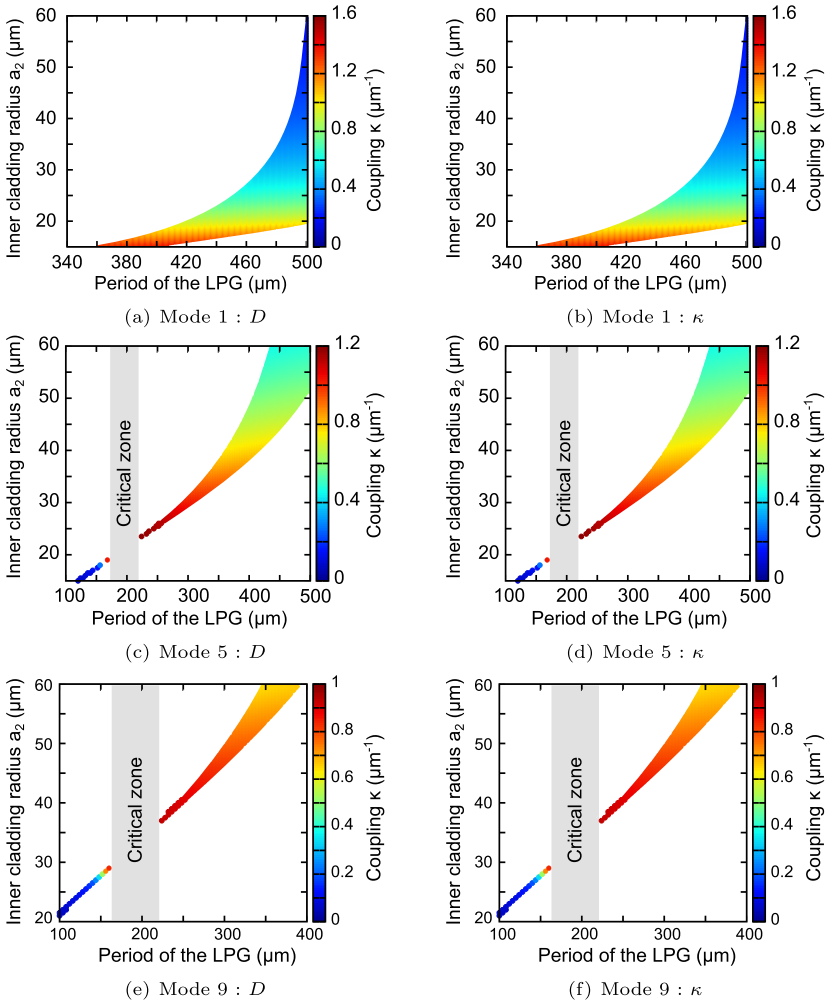

(a) Mode 1 : D (b) Mode 1 : κ

(c) Mode 5 : D (d) Mode 5 : κ

(e) Mode 9 : D (f) Mode 9 : κ

Fig. 5. Evolution of D and κ as a function of a_2 and Λ_{LPG}.

As stated by (16), the highest sensitivity is obtained with the largest values of D. For each mode, the largest values of D are located in the tip of the comma, *i.e.* for the smallest values of Λ_{LPG} and the smallest values of a_2. What is very interesting is that the highest coupling coefficients are also localized at the tip of the comma. This means that a couple $\{a_2, \Lambda_{\text{LPG}}\}$ can provide at the same time a good resolution and a good coupling.

However, it is not possible to choose the configuration with the highest D since other specifications have to be fulfilled. In particular, the shifts of wavelength must linearly evolve with the strain in the range $[-5000\ \mu\epsilon; +5000\ \mu\epsilon]$. In order to quantify the linearity of the behavior of the long-period grating, we use the estimate $C_{\text{moy}} = (|C_{\epsilon_r}| + |C_{\epsilon_z}|)/2$ where C_{ϵ_r} and C_{ϵ_z} are defined as:

$$C_\epsilon = \left[\sum_{i=0}^{N} (\epsilon_i - \overline{\epsilon_i}) \left(\Delta\lambda_{\text{LPG}}^m - \overline{\Delta\lambda_{\text{LPG}}^m}\right)\right] \left[\sum_{i=0}^{N} (\epsilon_i - \overline{\epsilon_i})^2 \left(\Delta\lambda_{\text{LPG}}^m(\epsilon_i) - \overline{\Delta\lambda_{\text{LPG}}^m}\right)^2\right]^{-\frac{1}{2}} \tag{17}$$

where N is the number of samples of strain ϵ_i for which $\Delta\lambda_{\text{LPG}}^m$ was calculated and $\bar{x}$ is the mean value of x. The parameter C_ϵ is the linear correlation coefficient, its value is between -1 and 1. The more $|C_\epsilon|$ is close to 1, the more the wavelength shift $\Delta\lambda_{\text{LPG}}^m$ is linear with the strain ϵ.

Fig. 6a shows the estimate C_{moy} as a function of D for modes 1 to 9. Surprisingly, the values are placed on the same curve for all the modes. This curve presents a maximum for $D = 1.75\ \text{pm}^2/\mu\epsilon^2$. We choose this value for the sensor. This is not a sufficient condition to fix the couple $\{a_2, \Lambda_{\text{LPG}}\}$, so we require a complimentary condition: $\lambda_{\text{LPG}} = 1.55\ \mu\text{m}$. This value is far enough from λ_{FBG}, so that no collapsing can occur between the FBG and the LPG resonant wavelengths when the strain increases.

The dark lines on the graphics in Fig. 6 correspond to the points where $D = 1.75\ \text{pm}^2/\mu\epsilon^2$ and the blue lines to the points where $\lambda_{\text{LPG}} = 1.55\ \mu\text{m}$. The intersections between these lines give the couples $\{a_2, \Lambda_{\text{LPG}}\}$ that meet all the require-

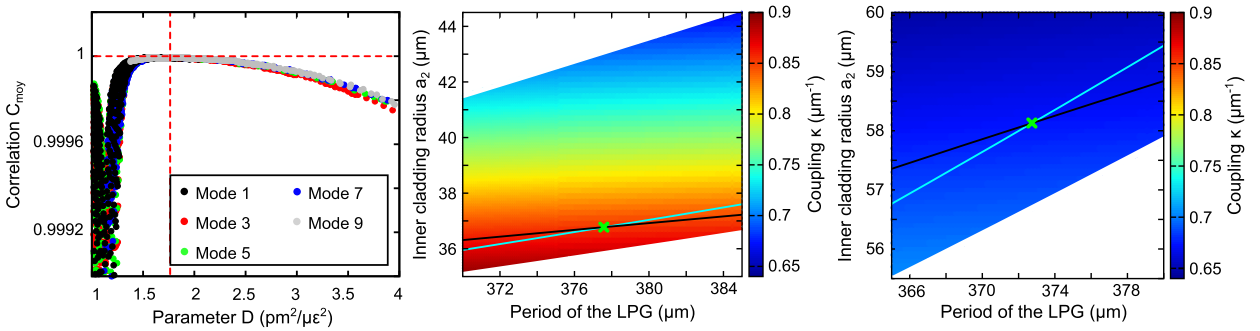

(a) Evolution of C_{moy} as a function of D. (b) $m = 5$ (c) $m = 9$

Fig. 6. Determination of the optimal configuration for different modes.

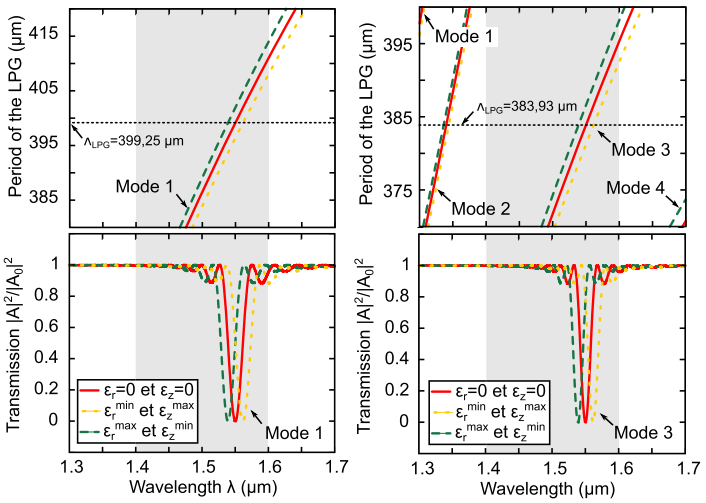

(a) LPG1 (b) LPG2

Table 2

m	a_2 (μm)	Λ_{LPG} (μm)	κ^m (μm^{-1})	α_{2r} ($pm/\mu\epsilon$)	α_{2z} ($pm/\mu\epsilon$)
1	15.45	399.25	1.33	−1.89	0.43
3	26.14	383.93	1.02	−1.86	0.42
5	36.78	377.65	0.85	−1.85	0.41
7	47.45	374.55	0.75	−1.85	0.41
9	58.13	372.77	0.68	−1.75	0.41

(c) Characteristics of the optimal long period gratings

Fig. 7. Optimal gratings.

ments. Table 2 summarizes the characteristics of long-period gratings given by these intersections for the five first modes. All these gratings present very similar sensitivities α_{2r} and α_{2z} and close periods Λ_{LPG}. In contrast, they exhibit quite different coupling coefficients. The coupling coefficients of mode 1 are almost twice the coupling coefficient of mode 9. Moreover, the radius of the inner cladding for mode 1 is smaller than those of other modes, which makes it less sensitive to bending. That is an other interesting feature.

At this step, we retain two configurations: LPG1: $\{a_{20} = 15.45\ \mu\text{m},\ \Lambda_{\text{LPG}} = 399.25\ \mu\text{m}\}$ with mode $m = 1$ and LPG2: $\{a_{20} = 26.14\ \mu\text{m},\ \Lambda_{\text{LPG}} = 383.93\ \mu\text{m}\}$ with mode $m = 3$. The last requirement that they have to fulfill is to present a single peak in the range [1400 nm; 1600 nm] whatever the strain.

Figs. 7 show the transmission spectrum of LPG1 and LPG2 together with the variation of the resonant wavelength as a function of the period of the grating: the straight line corresponds to the variation when the grating is at rest and the dashed lines to the maximum redshift and the maximum blueshift. The lengths of the gratings have been chosen to maximize the depth of the hole in the transmission spectrum. For LPG1, mode 1 is the only one resonant in the desired wavelength range. In fact, no other mode is resonant in the range of wavelengths [1300 nm, 1700 nm] for the considered range of strain $[-5000\ \mu\epsilon; +5000\ \mu\epsilon]$. For LPG2, we can see that modes 2 and 4 are close to the border. However, these modes do not interfere since their coupling coefficients are negligible. These two configurations can then be used.

We finally present in Fig. 8 the whole spectrum of the sensor with LPG1. The green solid line corresponds to the sensor at rest, the blue dash-dot line to the strain that gives a maximal blueshift and the red dashed line to the strain that gives a maximal redshift. We can notice a slight shift of λ_{LPG} in the absence of strain. This shift is due to the juxtaposition of the FBG. We can also notice the apparition of several narrow holes for wavelengths smaller than λ_{B}. These holes correspond to the coupling between cladding modes and the core mode induced by the FBG. However, these complementary holes do not induce confusion since their wavelengths are always smaller than λ_{B}.

Fig. 8 shows the variation of the wavelength shifts of the FBG and the LPG as a function of ε_z and ε_z. As expected, the response of the sensor is quite linear. The deviation from linearity does not exceed 50 $\mu\epsilon$ for a strain of 5000 $\mu\epsilon$, i.e. 1%. The sensitivity of the FBG to the axial strain is $\alpha_{1z} = 1.068$ pm/$\mu\epsilon$, and the one of the LPG is $\alpha_{2z} = 0.434$ pm/$\mu\epsilon$. The sensitivity

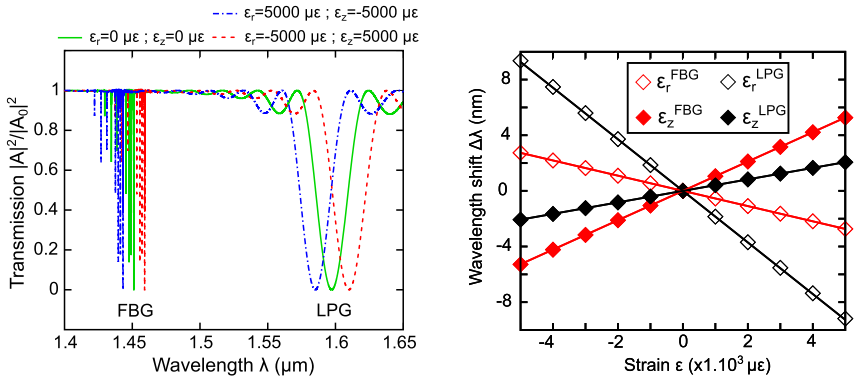

(a) Transmission spectrum of optimal sensor (b) Wavelength shifts vs. strain

Fig. 8. Response of the sensor to axial and radial strains.

of the FBG to the radial strain is $\alpha_{1r} = -0.555$ pm/με and the one of the LPG is $\alpha_{2r} = -1.895$ pm/με. From this values, and assuming that the smallest measurable wavelength shift is 1 pm, we deduce from (16) that the smallest measurable radial strain is $\Delta\epsilon_r = 1.4$ με and the smallest measurable axial strain is $\Delta\epsilon_z = 0.85$ με.

5. Conclusion

In this article, we studied an optical fiber sensor designed to discriminate axial and radial strains when embedded in a material host. The sensor is made of the juxtaposition of a fiber Bragg grating and of a long-period grating inside the core of a three-layer optical fiber. The specifications were designed to obtain a linear response of the sensor and a resolution similar to that of the classical strain gauge for the axial strain resolution, i.e. 1 micro-strain. Among all the parameters, we identified two relevant ones: the radius of the inner cladding and the period of the long-period grating. We then searched optimal values of these parameters and found several configurations. The most promising ones are associated with cladding mode orders 1 and 3. These configurations present smaller radii of inner cladding, which makes the sensor less sensitive to bending, and higher coupling coefficients that allow smaller lengths for the gratings. They allow us to measure the axial strain with a resolution of 0.85 με and the radial strain with a resolution of 1.4 με. This result is a real advance in strain measurement, since a classical embedded strain fiber sensor can not discriminate axial and radial strain. Moreover, the resolution on axial strain of a FBG mounted on a surface is of the order of 1 με. The range of measurable strain with a linear response is [−5000 με; +5000 με]. In this range, the deviation from linearity is less than 1%. All these properties can make this sensor a very useful tool for the measurement of strain inside structures. The next step is to investigate its sensitivity to bending.

References

[1] T.H.T. Chan, L. Yu, H.Y. Tam, Y.Q. Ni, S.Y. Liu, W.H. Chung, L.K. Cheng, Fiber Bragg grating sensors for structural health monitoring of Tsing Ma bridge: background and experimental observation, Eng. Struct. 28 (5) (2006) 648–659.
[2] R. Ramly, W. Kuntjoro, M.K. Abd Rahman, Using embedded fiber Bragg grating (FBG) sensors in smart aircraft structure materials, in: International Symposium on Robotics and Intelligent Sensors 2012 (IRIS 2012), Proc. Eng. 41 (2012) 600–606.
[3] F. Surre, R.H. Scott, P. Banerji, P.A.M. Basheer, T. Sun, K.T.V. Grattan, Study of reliability of fibre Bragg grating fibre optic strain sensors for field-test applications, Sens. Actuators A, Phys. 185 (2012) 8–16.
[4] Y.M. Gebremichael, W. Li, W.J.O. Boyle, B.T. Meggitt, K.T.V. Grattan, B. McKinley, G.F. Fernando, G. Kister, D. Winter, L. Canning, S. Luke, Integration and assessment of fibre Bragg grating sensors in an all-fibre reinforced polymer composite road bridge, Sens. Actuators A, Phys. 118 (1) (2005) 78–85.
[5] M. Bocciolone, G. Bucca, A. Collina, L. Comolli, Pantograph–catenary monitoring by means of fibre Bragg grating sensors: results from tests in an underground line, Mech. Syst. Signal Process. 41 (1–2) (2013) 226–238.
[6] R. Gafsi, M.A. El-Sherif, Analysis of induced-birefringence effects on fiber Bragg gratings, Opt. Fiber Technol. 6 (3) (2000) 299–323.
[7] M.S. Müller, C.D.A. Schnarr, Analytical coherency matrix treatment of shear strained fiber Bragg gratings, Opt. Express 17 (2009) 22624.
[8] M.G. Xu, J.-L. Archambault, L. Reekie, J.P. Dakin, Discrimination between strain and temperature effects using dual-wavelength fibre grating sensors, Electron. Lett. 30 (13) (1994) 1085–1087.
[9] E. Udd, Review of multi-parameter fiber grating sensors, in: Optics East 2007, International Society for Optics and Photonics, 2007, 677002.
[10] T. Mawatari, D. Nelson, A multi-parameter Bragg grating fiber optic sensor and triaxial strain measurement, Smart Mater. Struct. 17 (3) (2008) 035033.
[11] B.-O. Guan, H.-Y. Tam, X.-M. Tao, X.-Y. Dong, Simultaneous strain and temperature measurement using a superstructure fiber Bragg grating, IEEE Photonics Technol. Lett. 12 (6) (2000) 675–677.
[12] H. Chi, X.-M. Tao, D.-X. Yang, K.-S. Chen, Simultaneous measurement of axial strain, temperature, and transverse load by a superstructure fiber grating, Opt. Lett. 26 (24) (Dec 2001) 1949–1951.
[13] S. Triollet, Développement d'un capteur à fibre optique à base de réseaux de Bragg superposés de courtes et de longues périodes : application à la mesure discriminée de température et de déformation, PhD thesis, Saint-Étienne, France, 2010.
[14] D. Leduc, Y. Lecieux, P.-A. Morvan, C. Lupi, Architecture of optical fiber sensor for the simultaneous measurement of axial and radial strains, Smart Mater. Struct. 22 (7) (2013) 075002.
[15] V. Bhatia, Properties and sensing applications of long-period gratings, PhD thesis, Virginia Tech. Blackburg, VA, USA, 1996.

[16] S. Timoshenko, J.N. Goodier, Theory of Elasticity, McGraw-Hill, 1969.
[17] I. De Baere, E. Voet, W. Van Paepegem, J. Vlekken, V. Cnudde, B. Masschaele, J. Degrieck, Strain monitoring in thermoplastic composites with optical fiber sensors: embedding process, visualization with micro-tomography, and fatigue results, J. Thermoplast. Compos. Mater. 20 (5) (2007) 453–472.
[18] A. Bertholds, R. Dandliker, Determination of the individual strain-optic coefficients in single-mode optical fibers, J. Lightwave Technol. 6 (17) (1988).
[19] I. Krucinska, T. Stypka, Direct measurement of the axial Poisson's ratio of single carbon fibres, Compos. Sci. Technol. 41 (1) (1991) 1–12.
[20] L. Khoun, R. Oliveira, V. Michaud, P. Hubert, Investigation of process-induced strains development by fibre Bragg grating sensors in resin transfer moulded composites, Composites, Part A, Appl. Sci. Manuf. 42 (3) (2011) 274–282.
[21] S. Triollet, L. Robert, E. Marin, Y. Ouerdane, Discriminated measures of strain and temperature in metallic specimen with embedded superimposed long and short fibre Bragg gratings, Meas. Sci. Technol. 22 (1) (2011) 015202.
[22] T. Erdogan, Cladding-mode resonances in short- and long-period fiber grating filters, J. Opt. Soc. Am. A 14 (1997) 1760–1773.
[23] H. Kogelnik, Theory of dielectric waveguides, in: Integrated Optics, Springer, 1975, pp. 13–81.